RSC Advances

PAPER

View Article Online
View Journal | View Issue



Cite this: *RSC Adv.*, 2025, **15**, 26253

# Architecture of ytterbium selenite nanorods: unlocking structural, optical, magnetic and electrochemical behaviour with boosting performance for supercapacitors

S. Shanmugha Soundare, [a] S. Ariponnammal, [b] M. Arivanandhan [a] and R. Jayavel *[ac]

Ytterbium selenite ($Yb_2Se_3O_9$) was successfully synthesized using a simple coprecipitation technique, resulting in bamboo-like nanorods approximately 110 nm in size. The compound crystallizes in a monoclinic structure and exhibits promising features for optoelectronic applications and UV filtering. Spectroscopic analysis reveals native point defects as well as Schottky and Frankel surface defects, which facilitate radiative electron–hole recombination making it a potential material for display technologies. Ytterbium is embedded within an oxide matrix in the sample, and a distinct magnetic phase transition occurs between 20 K and 30 K under an applied magnetic field. At room temperature 300 K, the M–H curve indicates weak ferromagnetic behaviour. Electrochemical evaluation of $Yb_2Se_3O_9$ based electrodes in both symmetric and asymmetric supercapacitor configurations revealed impressive performance. The symmetric device exhibited a specific capacitance of 142.51 F $g^{-1}$, an energy density of 11.98 W h $kg^{-1}$, and a power density of 550 W $kg^{-1}$ at 1 A $g^{-1}$, with 78.09% capacitance retention after 10 000 cycles. Remarkably, the asymmetric supercapacitor achieved a higher specific capacitance of 169.86 F $g^{-1}$, an energy density of 60.39 W h $kg^{-1}$, and a power density of 800 W $kg^{-1}$ within a 1.60 V potential window, retaining 85% of its capacitance after 10 000 cycles. Impedance spectroscopy confirmed the material's double-layer capacitive behaviour. Overall, the asymmetric configuration demonstrated superior performance, making $Yb_2Se_3O_9$ a promising candidate for energy storage and conversion technologies.

Received 15th May 2025
Accepted 16th July 2025

DOI: 10.1039/d5ra03410h

rsc.li/rsc-advances



## Introduction

The two biggest problems facing humanity as its population grows are the energy crisis and environmental degradation. By 2050, it is projected that the globe will use roughly twice as many energy resources as it does now. The demand for environmentally friendly energy sources has grown in recent decades due to concerns about environmental contamination and fossil fuels depletion.[1,2] The scientific world is searching for effective renewable energy sources with storage capacities as a result of the growing demand for energy.[3] In global setting, sustainable development research has increasingly focused on energy. It is now imperative that more effective energy storage systems or technologies be developed and refined. In response to growing need of renewable sustainable energy sources, there have been attempts to produce devices for energy storage of lightweight, flexible, and eco-friendly. Thus, an energy storage device should meet necessary specifications, including those related to high power, energy density, portability, light weight, affordability, and long shelf life. The best technology for storing energy is a supercapacitor (SC). They are designed to generate devices for storing energy with intermediate specific energy that charge rapidly by completing the gap that batteries and capacitors left. When high power, fast charge–discharge, prolonged life cycle, and great reversible nature are needed, it is better to use supercapacitors (SCs) rather than batteries.[2] SCs are sometimes referred to as electrochemical capacitors. They are widely used in variety of power-saving industries, including portable electronics and continuous power transfers.[4–8] High specific power, remarkable capacitance retention (stability), and fast charge/discharge capability are the unique advantages of SCs.[9] Despite all of these benefits, SCs suffer from low specific energy, which hinders development.[10] In SCs, electrode materials are typically essential because they store charge at a point where the electrode and electrolyte meet. Therefore, capacitance and enactment of the electrodes are greatly influenced by the electrode materials' organized structure and unique surface characteristics.[11,12] For example, ion loading, movement and

[a]*Centre for Nanoscience and Technology, Anna University, Chennai 600025, Tamilnadu, India. E-mail: rjvel@annauniv.edu*

[b]*Department of Physics, Gandhigram Rural Institute, Deemed to Be University, Gandhigram, 624302, Dindigul District, Tamilnadu, India. E-mail: ariponnammal@gmail.com*

[c]*Crystal Growth Centre, Anna University, Chennai 600025, Tamilnadu, India*

transit, all of which determine the rate, effectiveness, and implementation of the materials used for the SCs electrodes. They were significantly influenced by the distribution of pore sizes in SC electrodes. In order to create a SC electrode with exceptional behaviour, it is crucial to achieve the special design and configuration for electroactive materials.[13] They fall into three categories: pseudocapacitors, hybrid and electric double layer (EDLC). Through quick, reversible electrochemical redox processes, the pseudocapacitors store energy. EDLC conserves energy by building up charge at electrode–electrolyte contact. EDLC preserves energy. Hybrid supercapacitors which are hybrid in nature combine benefits of EDLC and faradaic charge storage techniques. Researchers are looking for new materials that have incredible qualities like a huge surface area, variety of structure, a gentle porous nature, and the ability to change size of pore.[4] Chalcogenide and metal oxide-based materials have also attracted attention. Higher energy densities are possible with materials like molybdenum di sulfide, titanium oxide, and tin oxide. However, issues with inadequate cycling stability, volume expansion, and limited electrical conductivity need to be fixed if they realize their potential use in the realistic world. The material's many active patches, short ion diffusion channels, and high specific surface area (SSA) all contribute to its quick charge storage.[14] Polymers that are conducting and oxides of metals are suitable materials for electrodes in potential supercapacitor. The specific capacitance ($C_s$) of metal oxides is large. Despite being widely accessible and having a variety of oxidation states, conductive polymers have poor cycle stability and mechanical strength.[5] Furthermore, materials with defects can be used in battery, photo catalytic, electro catalytic, and thermal applications. Metal oxides are chemically stable and extensively distributed. They are affordably priced and have a distinctive electronic architecture. Usually, the flaws are advantageous to the materials. For instance, photo catalysis, energy storage, and electro catalysis all depend on oxygen vacancies.[6,7] Because condensed framework compounds can display a wide variety of cation configurations, their design in material science leads to the creation of unique physical properties.[8] The structural adaptability can be achieved by altering the framework's anionic moiety in addition to altering the cations, according to recent studies. Notably, the crystal structure of these compounds can be significantly influenced by the widespread existence of an electron pair on selenium(IV) centers that are stereochemically active. The need for unoccupied space for the single-pair electron of selenium has an impact on the overall structure. Therefore, it is expected that metal selenites will have rich structural chemistry when the naturally asymmetric $(SeO_3)^{2-}$ group is combined with different metals.[9–11] Chemical and material scientists have been interested in studying metal selenite in recent years.[10] Numerous earlier studies have examined the transition metal–selenium–oxygen system.[10] Selenium in oxidation state +IV is detected in a number of phases. In this manner, compounds of transition metal that contain oxoanions $(SeO_3)^{2-}$, $(HSeO_3)^{-}$ and $(Se_2O_5)^{2-}$ have been identified.[12,15] Many crystal structures associated with selenite compounds have been determined. Several phases' thermal behaviour and infrared spectroscopy have been documented.[11] The presence of antiferromagnetic interaction is demonstrated by the chain-structured $M(Se_2O_5)$ molecule.[11] An incredible range of inorganic networks templated by organic species, has been achieved by the use of mild hydrothermal methods under autogenous pressure.[11] It has been reported that two open structure selenites of zinc and iron(III) have been prepared using organic templates.[11] Recent reports have revealed the physical characteristics of manganese selenites, which were synthesized using moderate hydrothermal techniques.[12] Two polymorphs of $Mn(SeO_3)$ that were created under supercritical circumstances have also been studied for their crystal structure and physical characteristics.[12] Lanthanide ions ($Ln^{3+}$) differ from ordinary transition metal ions in that they have a high +3 charge and a large ionic radius which enable them to have good stability and strong coordinated bonding. This makes lanthanide metal–organic frameworks capable of producing faradaic redox reactions with high charge during the charge storage process as well as strong cyclic stability. Strong framework stability and flexible coordination chemistry make metal organic frameworks containing lanthanide ions attractive.[4] A hybrid metal–organic framework, consisting of centers of organic linker, samarium and thulium, coated over electrode of Ni-foam has high specific capacities with remarkable cycle stability.[4]

Rare earth-based nanomaterials and their composites have recently attracted the attention of researchers due to their uncommon unpaired 4f electronic configuration, controllable structure, and outstanding physical and molecular properties. With unique 4f electron configurations and a range of valences, the trivalent rare earth ions ($RE^{3+}$) are the most prevalent of the rare-earth (RE) elements' unique structures and properties.[16] Unpaired 4f electrons of $RE^{3+}$ provide unique energy storage capabilities since they typically do not establish chemical bonds.[17] Because of their advantageous redox characteristics and environmental friendliness, rare-earth-based nanomaterials, such as rare-earth sulfides, oxides, and hydroxides, have attracted a lot of attention. Co-precipitation, sol–gel, and hydrothermal procedures are examples of economical, scalable, and ecologically benign synthetic methods that can yield rare-earth-based nanomaterials with significant electrochemical properties. They are heavily utilized in three primary domains: clean energy, lifestyle, and defence. The market demand for RE elements is expected to increase due to the rising popularity of autos and electronic devices, as well as the recent growth of renewable energy alternatives to fossil fuels.[18] Because of its favourable characteristics, attractive magnetic properties, coordination chemistry, fair electronic arrangement, and energy storage capabilities, the research community is closely monitoring rareearth based components. $Ce^{3+}$, $Yb^{3+}$, and $Er^{3+}$ are a few valence cations studied for colloidal SCs. In the synthesis of rareearth based metal oxides, achieving a desired nanostructure with physico-chemical properties and effective surface area remains a difficult problem. Recently, analogous bimetallic oxides $TmSeO_3$, $TmTeO_3$, $Gd_2Se_3O_9$, $GdTeO_3$, and $YbTeO_6$ have been the subject of electrochemical studies.[15,19–22] The development of new electroactive materials is a relatively new discipline, and the search for active cathode materials is

 

a prominent topic in the rapidly expanding field of supercapacitors. The design of such a rareearth material with good electrochemical performance is the aspect that makes this paper innovative. As a result, ytterbium selenite was chosen for the present work's electrochemical analysis. Ytterbium is a member of lanthanides existing in +2 and +3 oxidation states. The more stable +2 oxidation state is enhanced by a virtually complete 4f electron shell. Furthermore, associated work on related compounds, such as selenite and tellurite of thulium and gadolinium has been reported recently.[15,19–21] Thus, a supercapacitor symmetrical and asymmetrical devices with $Yb_2Se_3O_9$ electrodes were constructed and tested by three and two electrodes system. This device has high density of power and energy, larger potential window, good stability of cyclic, and higher $C_s$ making it unique for applications related to conversion of energy and storage. Thus, in this paper, production of rare earth based electrode material ytterbium selenite $Yb_2Se_3O_9$ is made by using simple easy co-precipitation method and its characteristics have been presented in this paper.

## Methods and materials

The co-precipitation method (Fig. 1) is used to produce ytterbium selenite $Yb_2Se_3O_9$. The analytical-grade chemicals were supplied by Alfa Aesar. 30 milliliters of a 0.2 M $Na_2SeO_3$ and 30 milliliters of a 0.2 M $YbCl_3$ aqueous solution have prepared independently. The aqueous solution containing 0.2 M $Na_2SeO_3$ was added drop by drop consistently to 0.2 M $YbCl_3$ solution while being constantly swirled at 400 rpm for 8 h at 80 °C. After cooling, white precipitate forms. Ethanol and double-distilled water were used to regularly clean it after centrifugation. The precipitate was allowed to dry for few hours at temperature 50 ° C, then stored in desiccant.

English-made OXFORD INCAPENTAx3 model records energy dispersive X-ray analysis (EDAX), while the CAREL ZEISS EVO-18 type device captures scanning electron microscopy (SEM) and Thermofisher make Talos F200 S model captures transmission electron microscopy (TEM). PANalytical X'Pert Pro X-ray powder diffractometer (XRD) determine the structure using Cu Kα radiation, and particle size analyser Model Nano Plus and Make MICRIMERITICS measures the particle size. The ultraviolet-visible spectroscopy (UV-vis) is produced using a PerkinElmer Lambda 35 spectrophotometer, luminescence (PL) spectrum is obtained by VARIAN Cary Eclipse Fluorescence Spectrophotometer, the Fourier transform infrared (FTIR) spectrum is obtained by PerkinElmer and Raman spectrum is recorded by Bruker Multiram FT-Raman Spectrometer. The Thermo Fisher Scientific X-ray photoemission spectroscopy (XPS) BX model spectrophotometer records XPS spectra using Al Kα radiation (186.6 eV). Low-temperature magnetic measurements were conducted by Lakeshore model VSM 7410.

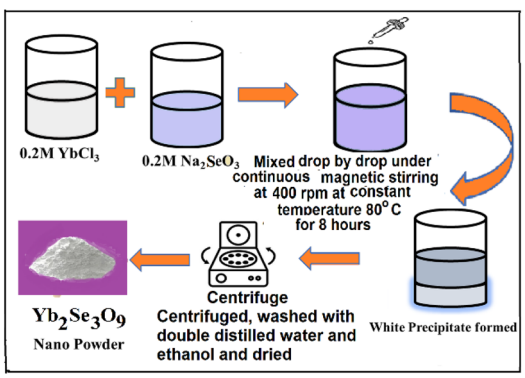


Fig. 1 Synthesis of $Yb_2Se_3O_9$ by co-precipitation process.

Electrochemical studies were conducted using the VMP-300 biological potentiostat integrated with EC-lab software. The generated materials were electrochemically analysed at room temperature. A mortar and pestle was used to pound 85 : 10 : 5 $Yb_2Se_3O_9$, carbon black and PVDF mixture to examine the electrochemical performance of ytterbium selenite. Few drops of *N*-methyl pyrrolidone solution (NMP) were then added to the mixture to completely mix it. A 1 $cm^2$ slurry coated Ni foam is allowed to dry. 3 M KOH electrolyte was used in this work. Three electrode cells tested the electrochemical characteristics of produced electrode of ytterbium selenite. Here, sample coated Ni foam, Ag/AgCl and platinum wire are working electrode, reference electrode, and counter electrode consecutively.

## Results and discussions

### Structure and surface morphology investigations

Fig. 2a portrays EDAX of ytterbium selenite $Yb_2Se_3O_9$. For ytterbium, selenium, and oxygen, the percentages of weight are 44.48%, 30.14%, and 25.38%, respectively (Fig. 2a), which correspond to the computed values of 44.65%, 30.57%, and 24.78%. The analysis confirms the constituents of $Yb_2Se_3O_9$. According to the EDS mapping, the sample's main constituents are ytterbium, selenium, and oxygen (Fig. 2b–d). This demonstrates that the sample is well formed and fully reacted. SEM picture of $Yb_2Se_3O_9$ (Fig. 2e) shows an interesting morphology of bundle of nanowires structure at 35k× and Fig. 2f shows nanorods with bamboo like structure at 100k× magnification. TEM picture at 100 nm and 50 nm (Fig. 2g and h) confirms nanorod structure. A particle size analyser has determined that the particle is 110 nm in size.

Fig. 3a depicts XRD pattern of $Yb_2Se_3O_9$. XRD peaks are indexed by least squares fit method confirming crystalline phase of the sample. It is of monoclinic structure with $a = 16.85 \pm 0.02$ Å, $b = 9.674 \pm 0.01$ Å, $c = 11.828 \pm 0.02$ Å, $\alpha = \gamma = 90°$, $\beta = 106.40°$ lattice parameters and $V = 1849.6$ Å$^3$ (JCPDS file no: 51-1788).

### XPS study

XPS study obtains chemical state bonding of Yb in ytterbium selenite. The ytterbium, selenium and oxygen elements are present in the ytterbium selenite survey spectrum, which is shown in Fig. 3b. The ytterbium related binding energy values are 401.9, 348.1, 186.7, and 28.3, and it displays the ytterbium elements $4p_{1/2}$, $4p_{3/2}$, $4d_{3/2}$, and $5p_{1/2}$. It also shows selenium elements 3s, $3p_{1/2}$, $3p_{3/2}$ and $3d_{3/2}$ at binding energies 234.3,

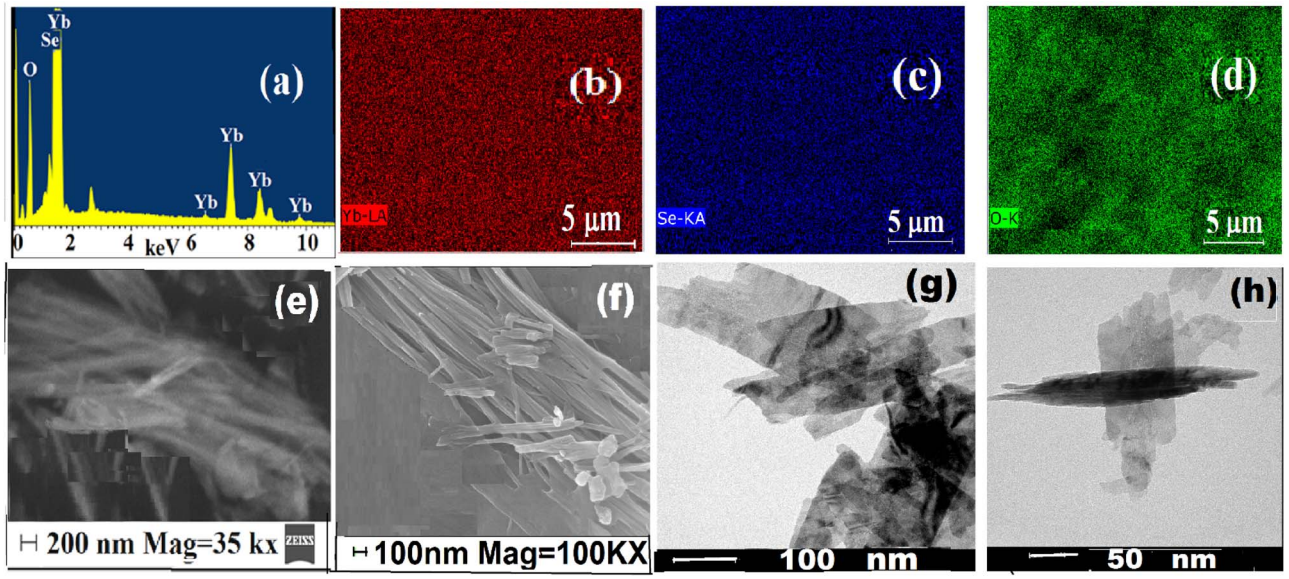


Fig. 2 (a) EDAX; EDS of (b) Yb, (c) Se, (d) O; SEM picture at (e) 35k× (f) 100k× and TEM picture at (g) 100 nm (h) 50 nm of $Yb_2Se_3O_9$.

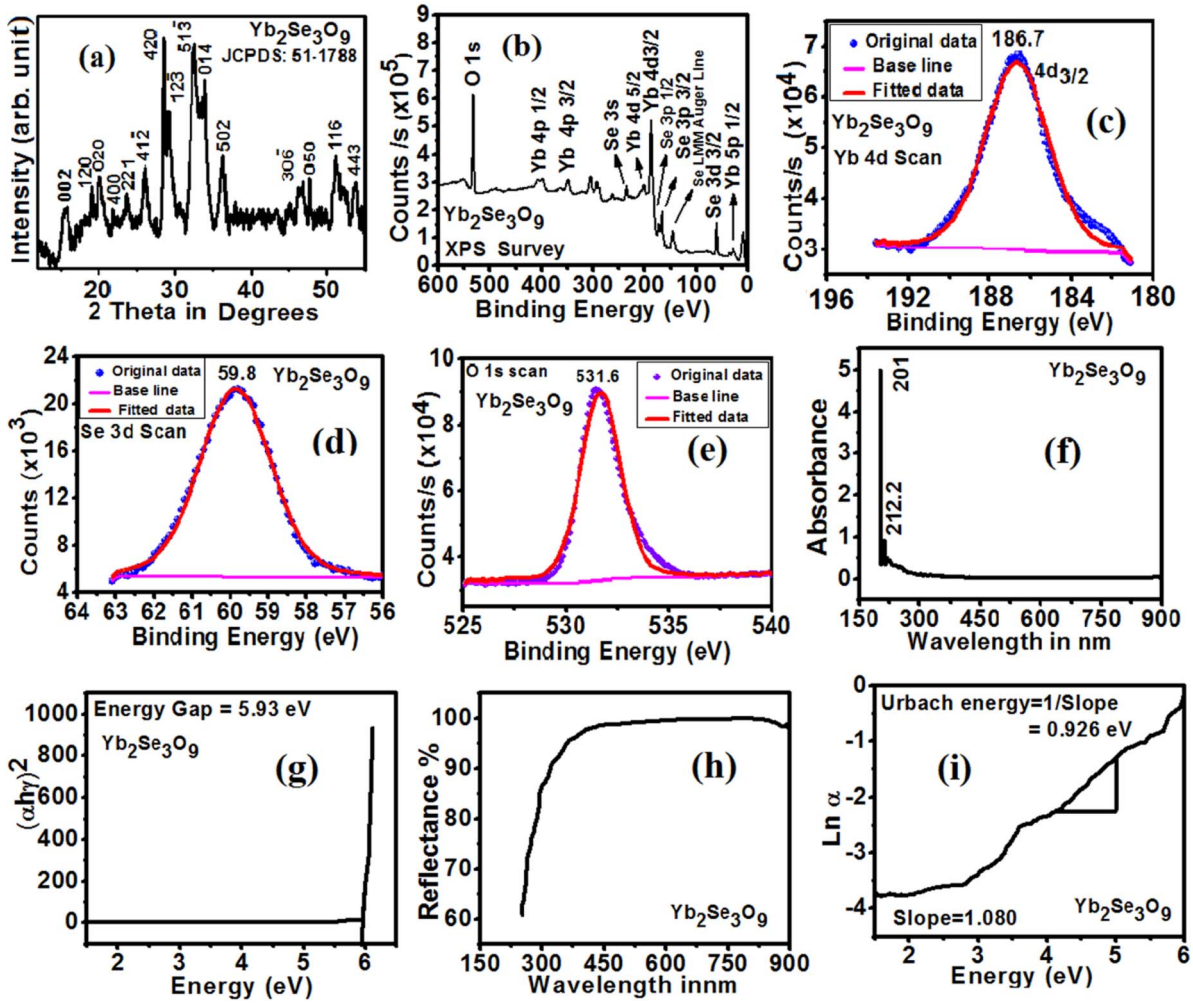


Fig. 3 (a) XRD, (b) XPS survey spectrum, (c) Yb 4d scan, (d) Se 3d scan, (e) O 1s scan, UV-visible (f) absorbance, (g) $(\alpha h\nu)^2$ *versus* energy plot, (h) reflectance (i) Urbach graph of $Yb_2Se_3O_9$.

171.1, 165.3 and 59.8 and oxygen 1s element at 531.6. Yb $4d_{3/2}$ is represented by the principal ytterbium signal of +3 valence at 186.7 eV in Fig. 3c. The detection of Yb $4d_{3/2}$ peaks in $Yb_2O_3$ [23–28] has verified the Yb existence in oxide matrix.[19] The peak at 59.8 eV BE in Selenium 3d spectrum (Fig. 3d) supports Se(II),- which is in line with previous findings of Se in selenite ($SeO_3$).[29] The production of Ytterbium oxide is suggested by oxygen 1s peak at 531.6 eV (Fig. 3e). The O 1s feature has a centre at 531.6 eV by metal oxide bond.[25,29]

## Optical studies

Fig. 3f depicts UV-visible spectrum exhibiting high absorption at about 201 nm then falls up to 204.5 nm and weak absorption at 212.2 nm. This make $Yb_2Se_3O_9$ appropriate for UV filter devices because of high UV absorption. Furthermore, from 263 to 900 nm, the visible area exhibits noticeably high transmittance. Tauc plot (Fig. 3g) gives energy gap 5.93 eV.[30] The spectrum of reflectance (Fig. 3h) between 404 to 900 nm shows the aforementioned absorbance trend. Because of this, $Yb_2Se_3O_9$ is a useful material in the optoelectronics industry. Peaks of absorption occurs beneath 250 nm due to 4f–5d electron transfer. The 201 nm peak represents the 4f–5d transition.[19,30] Urbach plot (Fig. 3h), Ln $\alpha$ *versus* energy gives Urbach energy 0.926 eV. Using relationship proposed by Sakka and Dimitrov,[7] refractive index '$n$' is 1.873 from optical energy gap '$E_{opt}$'.

$$\frac{n^2-1}{n^2+2} = 1 - \sqrt{\frac{E_{opt}}{20}}$$

The emission luminescence spectrum is displayed in Fig. 4a. Radiative and nonradiative centres can be seen in rareearth.[7] Due to native point defects, visible region shows mild green emission (~522.1 nm) and medium red emission (~789.0 nm) when excited at 390 nm, whereas the UV region shows strong efficient emission in (~388.8 nm).[31] A wide band in luminescence spectrum is associated with defects in the visible region, whereas an ultraviolet emission band is with emission of near band-edge (NBE)[32] caused by exciton recombination from a conduction-confined level to the valence band. As a result, NBE emission at 388.8 nm is resulted due to recombination by radiation of the valence hole and conduction electron.[7] The PL peak in the spectrum at about 388.8 nm is caused by NBE recombination involving excitons in $Yb_2Se_3O_9$, but its second order peak at roughly 789 nm. Generally, crystallizing circumstances are the occurrence of visible region emission.[32] Different Frenkel and Schottky surface imperfections are responsible for emission peak in visible region.[33] In oxide systems, interstitials and vacancies of oxygen significantly affects luminescence response.[33] According to reports, $Yb_2O_3$ nanoparticles exhibit eight enhanced luminescence emissions in the 405–600 nm range, as a result of electron's transfer from $^5D_J$ to $^7F_{J'}$ ($J = 0,1,2$ and $J' = 1$–3).[33] At 424, 440, 455, 474, 502, 557, 568, and 583 nm, three different emission peaks were detected: blue ($^5D_2$ to $^7F_{0,1,2,3}$), green ($^5D_1$ to $^7F_{0,1,3}$), and yellow ($^5D_0$ to $^7F_1$). These peaks correspond to their respective values. Emission maxima were seen around 520.4 nm as a result of the electrons' passage from the states $^5D_0$ to $^7F_1$.[23] Wang proposes that near the conduction band, recombination of delocalized electron with a surface oxygen vacancy in a single charged state causes photoluminescence's UV emission in a deep band at roughly 388.8 nm [24] which enhances potential use in displays. Variations in PL intensities can result from different fuels triggering differing oxygen vacancy densities. Ultraviolet peak may also be due to $Yb_2Se_3O_9$'s electron–hole radiation recombination. Nanoparticles are likely to be used in luminescence, optoelectronic devices, and UV photo-conductive detectors.[25]

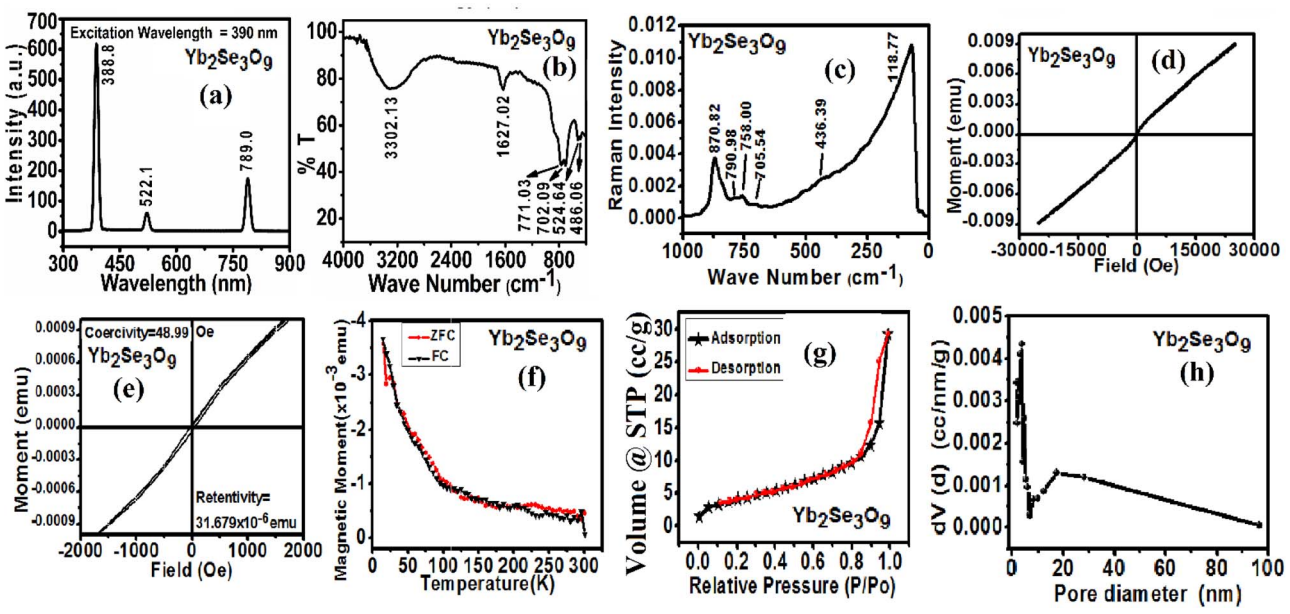


Fig. 4 (a) PL, (b) FTIR spectrum; (c) Raman (d) M–H curve at 300 K, (e) expanded M–H curve at 300 K, (f) ZFC and FC magnetic curve; (g) isotherm curve and (h) distribution of pore size of $Yb_2Se_3O_9$.

Fig. 4b shows spectrum of FTIR of $Yb_2Se_3O_9$. The hydroxyl group linking Yb is represented by the broad trough with a centre at 3302.13 $cm^{-1}$ .[26,27,34,35] The Yb–O stretching bond in deformed $YbO_6$ octahedrons and deformation bridge bond's stretching vibrations Yb–O–Yb or O–Yb–O are responsible for the band at 524.64.[26,27,34] Presence of O–H band appears at 1627.02 $cm^{-1}$ hint the hygroscopic sample nature.[35–37] Finger print region bands at 771.03, 702.09 and 486.06 $cm^{-1}$ confirms presence of Se–O band.[24,38–40]

Raman spectrum for ytterbium selenite $Yb_2(SeO_3)_3$ has been assigned as in Fig. 4c. Four fundamental vibrational frequencies are present in a free selenite ion with $C_{3v}$ symmetry: the doubly degenerate modes ϒ3 and ϒ4 at 740 and 374 $cm^{-1}$, respectively, and the non-degenerate symmetric stretching and bending modes ϒ1 and ϒ2 at 810 and 425 $cm^{-1}$[41] These foundational concepts are all Raman active. The non-degenerate symmetric stretching vibrations of the $SeO_3^{2-}$ ion are responsible for the strong Raman bands seen in the 780–896 $cm^{-1}$ area. The non-degenerate symmetric stretching vibrations of $SeO_3^{2-}$ ions are responsible for the strong band at 870.82 $cm^{-1}$ and the weakly intense one at 790.98 $cm^{-1}$.[41] Translational and rotational modes could be the cause of the lines seen between 300 and 79 $cm^{-1}$. Generally speaking, rotational modes should be more intense and have a greater wavenumber than translational modes. Rare-earth ion translational modes are responsible for medium-intense band seen at 118.77 $cm^{-1}$.[42] The band at 436.39 and 705.54 correspond to Se–O stretching and Se–O–Se asymmetric stretching.[43] It has been reported that bands in the range 672–698, 752–778 and 829–860 $cm^{-1}$ were assigned to Yb–O band. This confirms that the band at 758 corresponds to Yb–O.[44]

### Magnetic investigations at low temperatures

$Yb_2Se_3O_9$'s M–H curve at 300 K in Fig. 4d shows that the material is paramagnetic and its enlarged M–H curve displayed in Fig. 4e, provide clues for weak ferromagnetic activity. Retentivity is 31.68 × $10^{-6}$ emu. Positive intrinsic coercivity is 48.99 Oe.

$Yb_2Se_3O_9$ shows complete reversible characteristics under magnetic field in temperature range 300 and 20 K that is field cooled (FC) and zero field cooled (ZFC) (Fig. 4f) susceptibility of magnetic field falls with increasing temperature until saturation is achieved. In cooling with zero field, a peak is seen between 20 and 30 K, indicating presence of phase transition. This might be the result of presence of little impurity in $Yb_2Se_3O_9$. Reports state that a cusp observed in $Gd_5Si_3$ close to 80 K implies that a small impurity is present. In $Gd_{0.75}Se$, a cusp is seen between 65 and 95 K. According to reports, it is exhibited due to minute impurity presence or onset of phase transition.[29,45]

The applied 2000 Oe field, aligned nearly all spins of ytterbium by field cooling resulting cooperative interaction of ytterbium spin and sample's magnetization gets saturated.

### BET study

Utilizing Brunauer–Emmett–Teller (BET) study, sample's properties of surface were ascertained. Pore size distribution and surface area have been evaluated for $Yb_2Se_3O_9$ using the nitrogen adsorption–desorption method. Fig. 4g shows hysteresis loop of type IV in $Yb_2Se_3O_9$ sample's isotherm profiles.

This suggests the material's structure of mesoporous nature. The $Yb_2Se_3O_9$ sample's notable improvements in $N_2$ adsorption and decreased pore size distribution raise the prospect of increased catalytic activity. The pore size distribution graph (Fig. 4h) of $Yb_2Se_3O_9$ by BJH approach was projected from $N_2$ adsorption–desorption branches. The peak is centered at 3.83 nm. The less pore size and more pore volume enable efficient electron transport across the electrode/electrolyte contact. It is well known that the pores can promote the growth of capacitance by making ion movement easier and expanding the pool of electrolyte access.[46,47] According to reports, because of the increased pore capacity in the charging–discharging process, the electrolyte ions have greater accessibility area. Because of their short transport pathways and large number of redox active sites, well-developed pore structure favours energy storage. The pore channels provide more active sites for redox processes and boost up access of electrolyte. Both are advantageous for supercapacitors. The pore diameter of the $Yb_2Se_3O_9$ sample is 3.743 nm, its pore volume is 0.050 $cm^3$ $g^{-1}$, and its surface area is 21.537 $m^2$ $g^{-1}$. The $Yb_2Se_3O_9$ sample exhibits superior surface area and pore volume, advantageous for SCs applications, according to the BET analysis.

### Electrochemical investigations

At room temperature, the produced material $Yb_2Se_3O_9$ electrodes' supercapacitive behaviour was assessed. Cyclic voltammetry (CV) analysed redox processes generated by electrodes at various scan speeds. Charge–discharge and electron mobility, were also examined using charge–discharge and impedance spectroscopic studies using aqueous electrolyte of 3 M KOH.

### Three electrode configuration analysis

Cyclic voltammetry (CV) studies from 5 to 100 mV $s^{-1}$ scan speeds were acquired using three electrode arrangement. With a 3 M concentration KOH solution, the operational window is 0.65 V from the 0 to 0.65 V potential range and shows pseudocapacitive behaviour with reversible redox couple having good symmetry accompanying a single reduction signal from the $Yb^{3+}$ contribution and one unique oxidation peak from the selenite contribution (Fig. 5a). Specific capacitance decreases with increase of scan rate (Fig. 5b). One can describe the redox mechanism as follows. The main source of the pseudo capacitance for the $Yb_2Se_3O_9$ electrode is the reversible redox transfer between $Yb^{2+}$ and $Yb^{3+}$ at electrode/electrolyte contact.

The strong base electrolyte (KOH) and $Yb_2Se_3O_9$ undergo redox reaction. It is shown by the existence of a redox shoulder in CV plots, as shown in Fig. 4a, suggesting effective transmission of charge associated with $OH^-$ ions adsorption behaviour in $Yb_2Se_3O_9$ electrode. $Yb_2Se_3O_9$ becomes an electrochemically active species that allows for greater charge storage when it gets interacted with electrolyte KOH and becomes incorporated into metal oxides or hydroxides by surface chemical reconstruction. During faradaic charge

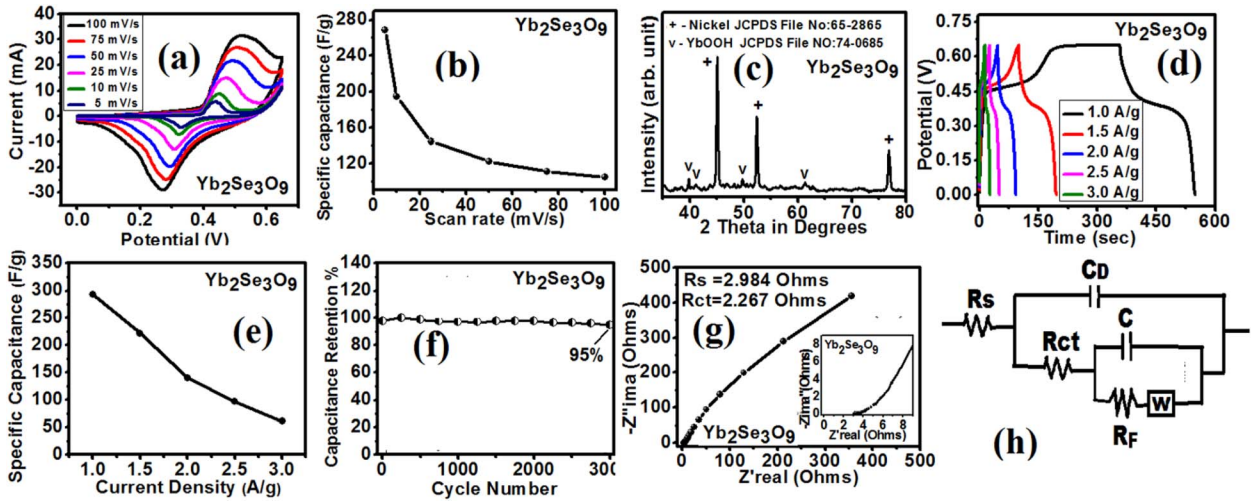


Fig. 5 (a) CV graph, (b) specific capacitance *versus* scan rate, (c) XRD of $Yb_2Se_3O_9$ electrode after electrochemical reaction in KOH electrolyte, (d) GCD curves, (e) specific capacitance *versus* current density, (f) cyclic stability, (g) Nyquist plot and (h) equivalent circuit of $Yb_2Se_3O_9$.

transfer process, $K^+$ ions distribute into the $Yb_2Se_3O_9$ structure. $Yb_2Se_3O_9$ showed the specific capacitances ($C_s$) 268.59, 194.73, 144.26, 121.80, 110.99 and 104.36 F $g^{-1}$ at 5, 10, 25, 50, 75 and 100 mV $s^{-1}$ scans (Fig. 4b). Furthermore, with scan speeds from 5 to 100 mV $s^{-1}$, CV curve area grows proportionately, suggesting that the electrode is capacitive. Additionally, even at higher scan speeds, the CV plot's shape essentially stays same, demonstrating $Yb_2Se_3O_9$'s strong rate and capacitance performance. Additionally, insufficient ion intercalation from the electrolyte into the dense centre of the nanostructure causes peaks of cathodic to migrate to reduced potential and peaks of anodic to travel to a higher potential. A comparatively rapid redox reactions and minimal resistance at interface are indicated by rising of density of current of anodic peak and falling of density of current of cathodic.[48] The reaction mechanism is

$$Yb^{3+} + 3OH^- \rightarrow YbOOH + H_2O$$

$$YbOOH + H_2O + e^- \leftrightarrow OH^- + Yb(OH)_2$$

$$Yb^{3+} + e^- \rightarrow Yb^{2+}$$

XRD data (Fig. 5c) shows Nickel peaks due to nickel foam and further confirm the formation of tiny YbOOH with faint diffraction peaks after the electrochemical reaction.

Chronopotentiometry study shows that galvanostatic charge/discharge (GCD) at current densities from 1 to 3 A $g^{-1}$ are nearly symmetric, showing a high efficiency of coulombic, as shown by Fig. 5d. It illustrates effects of highly reversible redox processes on the charge–discharge. Furthermore, electrochemical adsorption–desorption process and charge-transfer reaction at electrode/electrolyte interface cause voltage plateaus to exhibit their typical pseudocapacitive tendencies, agreeing with the redox peaks at all scan speeds in CV curves.[49] The $C_s$ fluctuation *versus* current densities is displayed in Fig. 5e. As current densities increased, capacitance decreased, which may be related to internal resistance of electrode material. At 1 A $g^{-1}$, $Yb_2Se_3O_9$ showed an outstanding $C_{sp}$ value of 292.82 F $g^{-1}$. For current 1.5, 2, 2.5 and 3 A $g^{-1}$, specific capacitance of $Yb_2Se_3O_9$ is 221.36, 140.19, 96.49, and 61.19 F $g^{-1}$ (Fig. 5e). The main cause of the high capacitance for $Yb_2Se_3O_9$ was pseudo behaviour in strong base electrolyte (3 M KOH), which was made possible by $Yb_2Se_3O_9$ that was uniformly impregnated on the nickel substrate's surface using a straightforward dip coating. Furthermore, during a redox reaction, a nickel substrate offers a more effective conductive channel for the intercalation and deintercalation of ions.[50]

Cyclic stability ascertains the range of its practical use. Cycle stability test was conducted on $Yb_2Se_3O_9$ for 3000 cycles at 5 A $g^{-1}$ and Fig. 5f shows stability curve of charge–discharge. Capacitance retention was calculated to be 95% for $Yb_2Se_3O_9$ sample 3000 cycles later.

Electrochemical impedance spectroscopy comprehend the mechanism of charge mobility and transfer of electron at electrode interface and it is employed. Nyquist plot and its equivalent fit circuits of $Yb_2Se_3O_9$ are displayed in Fig. 5g and h. Nyquist plot shows low series resistance $R_s$ = 2.984 Ω in high-frequency, indicating low electrode–electrolyte solution resistance. An electron-limited process produces high frequency region semicircle, whereas a diffusion-limited process produces a Warburg component with a long tail at lower frequencies. These two unique regions are visible in the Nyquist plot. These imply two mechanisms: kinetics and diffusion processes that control electrochemical performance of $Yb_2Se_3O_9$. Higher conductivity and quicker electron transfer are characteristics of material with low charge transfer resistance value ($R_{ct}$) 2.267 Ω.[50–58]

## Fabrication and analysis of $Yb_2Se_3O_9$ symmetric supercapacitor device

Symmetric $Yb_2Se_3O_9$//$Yb_2Se_3O_9$ supercapacitor device was constructed using electrolyte of 3 M concentration potassium

hydroxide and two $Yb_2Se_3O_9$ electrodes. Here $Yb_2Se_3O_9$ material coated Ni foam, acts as electrodes that are both positive and negative. A manual press was employed to compress prepared $Yb_2Se_3O_9$ electrodes. In symmetric device, an $Yb_2Se_3O_9$/NF electrode piece was used, along with a polyurethane foam separator and another piece of $Yb_2Se_3O_9$/NF ($1 \times 1$ cm$^2$) for the positive electrode. In the meantime, 3 M KOH electrolyte was used to soak the electrodes and separator for roughly two hours. Before sandwiching, considerable care was taken to ensure a fine layer of electrolyte soaked polyurethane foam to be fabricated on one side of both the $Yb_2Se_3O_9$/NF and $Yb_2Se_3O_9$/NF electrodes, ensuring an efficient separator's purpose and finally wrapped by adhesive tape. The experimental setup is straightforward and resembles the design of a pouch cell. Electrode, separator and electrode can be stacked layer by layer.

It connects commercial production of high-performing supercapacitors with tiny laboratory-scale testing. Each electrode's active material mass was determined to be 2 mg. Consequently, the symmetric device's active material had a total mass of 4 mg.

By cyclic voltammetry, after learning about the beneficial structural characteristics and compositional merits, electrochemical properties of as-fabricated $Yb_2Se_3O_9$ electrode was evaluated. The unique multiple oxidation states $Yb^+$, $Yb^{2+}$ and $Yb^{3+}$, allow greater reactions of redox, and high electrical conductivity. So, ytterbium-based compounds have the ability of more charge storage within larger potential window than other materials.[59] Examining the potential window of the electrolytes and CV plots of $Yb_2Se_3O_9$ electrode material, symmetrical SCs operating voltage is confined. Since potential and capacitance of a device are directly correlated with the amount of energy it stores, increasing operating voltage of SCs is essential. $Yb_2Se_3O_9$ electrodes showed a quasi-rectangular form, as shown in Fig. 6a, with the exception of the high potential, where the electrode material's instability was noticeable. The evolution reaction between hydrogen and oxygen is responsible for this, which narrows the operating voltage. Hence, electrochemical analysis in a symmetric supercapacitor was conducted using the identified operating potential of 1.1 V.[60] Non-rectangular shapes of the CV curves using 3 M KOH electrolyte at each 5 to 100 mV s$^{-1}$ scan, clearly show a highly conductive nature and reversible redox activity. To investigate the behaviour of $Yb_2Se_3O_9$//$Yb_2Se_3O_9$ device, the optimal behaviour of symmetric device SCs (Fig. 6a), is indicated by CV obtained inside window of potential 0 to 1.1 V, where an increase in current was detected in varied scan rates. Peaks may undergo sufficient shift, perhaps overlap with region of potential where evolution of hydrogen appears with higher sweep rates due to kinetic restrictions caused by the large reduction in the required time for reaction of redox to occur when the scan rate increased.[25] Additionally, form of CV plot shows electrode material's exceptional rate capacity and the device's durability against higher current ratings.

In chronopotentiometric analysis of GCD profile, materials' capacity to store charge was quantified. The constructed $Yb_2Se_3O_9$//$Yb_2Se_3O_9$ device's GCD graphs (Fig. 6b)at various current densities 1 to 3 A g$^{-1}$, in 1.1 V potential window, showed close symmetric nature, indicating redox processes continuity and efficacy at higher currents. Based on discharge, the symmetric device demonstrated high specific capacity of 142.51, 122.70, 102.08, 68.51 and 41.24 F g$^{-1}$ for 1, 1.5, 2, 2.5 and 3 A g$^{-1}$ current densities, correspondingly (Fig. 6c). The mesoporous structure with a high SSA is responsible for the $Yb_2Se_3O_9$ electrode's improved specific capacitance and superior electrochemical properties. Due to limitations of faradaic redox reactions at the electrode surface, capacity generally tends to degrade as current density rises.[48] A kinetic barrier that prevents $K^+$ ions in the electrolyte, from penetrating into active sites on the electrode material, results in less incoming ions being accessible on the electrode surface at high current densities because of time constraints. As a result, the specific capacitance decreases.[61]

Energy and power density are deciding parameters of device's capacity for energy storage. These relative parameters of $Yb_2Se_3O_9$//$Yb_2Se_3O_9$//KOH device are plotted in Ragone plot

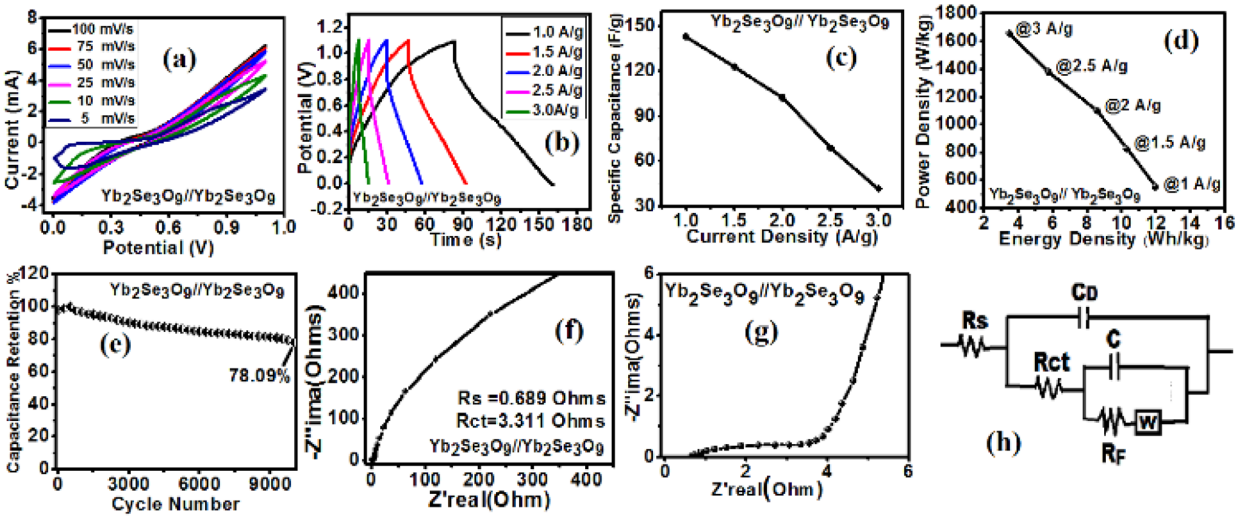


Fig. 6 (a) CV, (b) GCD, (c) $C_{sp}$ *versus* current density, (d) Ragone plot, (e) cyclic stability, (f) Nyquist plot, (g) expanded Nyquist plot and (h) equivalent circuit of symmetric $Yb_2Se_3O_9$//$Yb_2Se_3O_9$ device.

(Fig. 6d), were computed from the discharge profiles in order to examine the operational parameters.[62] At present $Yb_2Se_3O_9$// $Yb_2Se_3O_9$ symmetric device demonstrated a great power density 550 W kg$^{-1}$ and high energy density 11.98 W h kg$^{-1}$ at 1 A g$^{-1}$. Symmetric supercapacitor demonstrated significant energy density retention with increasing power density, achieving values of 10.31, 8.58, 5.76, and 3.47 W h kg$^{-1}$ at notable high density of power 825, 1100, 1375, and 1650 W kg$^{-1}$, respectively, at 1.5, 2, 2.5, and 3 A g$^{-1}$ current densities. Manufactured device's good electrochemical performance shows that nanoparticles and nanocomposite can efficiently boost ionic and electronic transport while lowering charge-transfer resistance.[63]

Cyclic stability is an essential need for supercapacitor devices for an extended electrochemical cycle life. Using GCD cycling at 5 A g$^{-1}$ upto ten thousand cycles, the $Yb_2Se_3O_9$// $Yb_2Se_3O_9$ symmetric capacitor operating at 1.1 V was tested for cycling performance. In Fig. 6e, the cycling stability is displayed. After 500 cycles, specific capacitance attained 100% retention and thereafter lowered, which can be linked to the electrode's surface wettability problems. Additionally, the deterioration of electroactive material results in detachment throughout GCD cycles may be source of specific capacitance decrement as cycle's number rises.[64] Symmetric capacitor has exceptional stability of cycle after 10 000 cycles with retention capacity 78.09%. For a faradaic-based system, this would be a favourable outcome, which permits the development of high-performing electrodes for the application of such unique and promising materials in consumer electronics.

Impedance analysis examines the capacitive and resistive parts of the supercapacitor device which investigates charge mobility, electron transport at electrolyte–electrode interface, and created resistance of the system. At higher frequencies, the charge-transfer resistance of electrodes and electrolytes is arranged in a semicircle. The diffusive resistance, sometimes referred to as Warburg impedance, is explained by the linear line. The obtained slope, which is more than 45°, shows that the electrode material has good capacitance. A series resistance of $R_s \sim 0.689\ \Omega$ was obtained from the intercept of real axis. In the high-frequency zone, at electrode and electrolyte interface, the Warburg impedance W, the double-layer capacitance C, and charge-transfer resistance $R_{ct} = 3.311\ \Omega$ regulate the process of impedance of electrolyte. For the generated nanoparticles, Fig. 6f and g show the Nyquist plot and expanded Nyquist plot. Equivalent circuit is shown in Fig. 6h. These exceptional qualities provide a viable path for investigating rare earth compounds as cutting-edge electrode materials for supercapacitor applications.[48]

### Asymmetric supercapacitor (ASC) device fabrication and performance assessment of $Yb_2Se_3O_9$

Asymmetric (ASC) $Yb_2Se_3O_9$//AC supercapacitor has been constructed as follows. A manual press was used to compress the constructed positive electrode of $Yb_2Se_3O_9$ and negative electrode of activated carbon. In negative electrode, an AC/NF electrode piece was used, along with a polyurethane foam separator and a piece of $Yb_2Se_3O_9$/NF (1 × 1 cm$^2$) for the positive electrode. In the meantime, 3 M KOH was used to soak the electrodes and separator for roughly two hours. Prior to sandwiching, great effort was taken to make sure, a fine layer of polyurethane foam soaked with 3 M KOH electrolyte was fabricated on one side of both electrodes $Yb_2Se_3O_9$/NF and AC/NF, assuring the aim of an effective separator and finally wrapped by adhesive tape. The layer positioned between the electrodes will stop the short circuit. Charge balance concept enhanced mass balancing of electrodes of negative and positive. Teflon tape was utilized to accurately seal the manufactured devices to provide a dependable function. The positive and negative electrodes' capacity to operate at high rates allowed us to create high-performing electrodes, which results use of novel electronic materials. Consequently, constructed asymmetric capacitor may reach high energy and power density.

Supercapacitor properties of $Yb_2Se_3O_9$//AC//KOH ASC is elaborated here. The elements crucial for determining electrochemical performance of materials from the standpoint of commercialization are: the three-electrode setup confirms that the $Yb_2Se_3O_9$ electrode exhibits better electrochemical characteristics with a larger capacitance and low charge transfer resistance. An ASC was constructed to evaluate electrochemical behaviour of the electrode $Yb_2Se_3O_9$ in two-electrode arrangement for commercial applications. The ASC is made up of activated carbon and $Yb_2Se_3O_9$. In this case, the cathode is $Yb_2Se_3O_9$, and the anode is AC in an electrolyte solution of 3 M KOH. An ASC with $Yb_2Se_3O_9$ cathode and AC anode was developed in order to actualize the electrochemical properties of $Yb_2Se_3O_9$ electrode. Its performance was then measured in two-electrode setup for practical uses. The individual electrodes were clubbed using 3 M KOH electrolyte soaked polyurethane foam separator, sandwiched between them to fabricate $Yb_2Se_3O_9$//activated carbon (AC)/KOH ASC. The layer cast in the middle of the electrodes will avert the short circuit. Also, positive and negative electrode mass balancing was enhanced by the charge balance hypothesis. Teflon tape was utilized to accurately seal the manufactured devices to provide a dependable function. The electrochemical performance of AC is discussed below.

Fig. 7a shows cyclic voltammetry plots of the AC and $Yb_2Se_3O_9$ electrodes. The AC EDLC trend is certified by rectangular curve, while the $Yb_2Se_3O_9$ shows a pseudocapacitive CV plot at 50 mV s$^{-1}$ scan. It determines ideal working potential of −1.0 to 0 V and 0 to 0.65 V by three-electrode cell. As a result, the oxygen evolution process began to manifest above 1.6 V, limiting the generated ASC in range that was the subject of the electrochemical analysis. Similarly, as illustrated in Fig. 7b, the $Yb_2Se_3O_9$//AC//KOH ASC broadens the frame of voltage by upto 1.6 V at 5 to 100 mV s$^{-1}$ scan. With quick diffusion and simple transport of ions of electrolyte to interface of electrode, excellent shaped CV curves are observed even at high 100 mV s$^{-1}$ scan.[65]

Device's performance was further assessed by chronopotentiometry charge–discharge test with various densities of current (Fig. 7c) 1, 1.5, 2, 2.5, and 3 A g$^{-1}$ in operating window of 0 to 1.6 V to provide a more thorough understanding of capability of sample electrodes for storage of energy. GCD curves' nearly symmetrical shape at different currents 1, 1.5, 2, 2.5 and 3 A g$^{-1}$ indicates the electrode material's good electrochemical

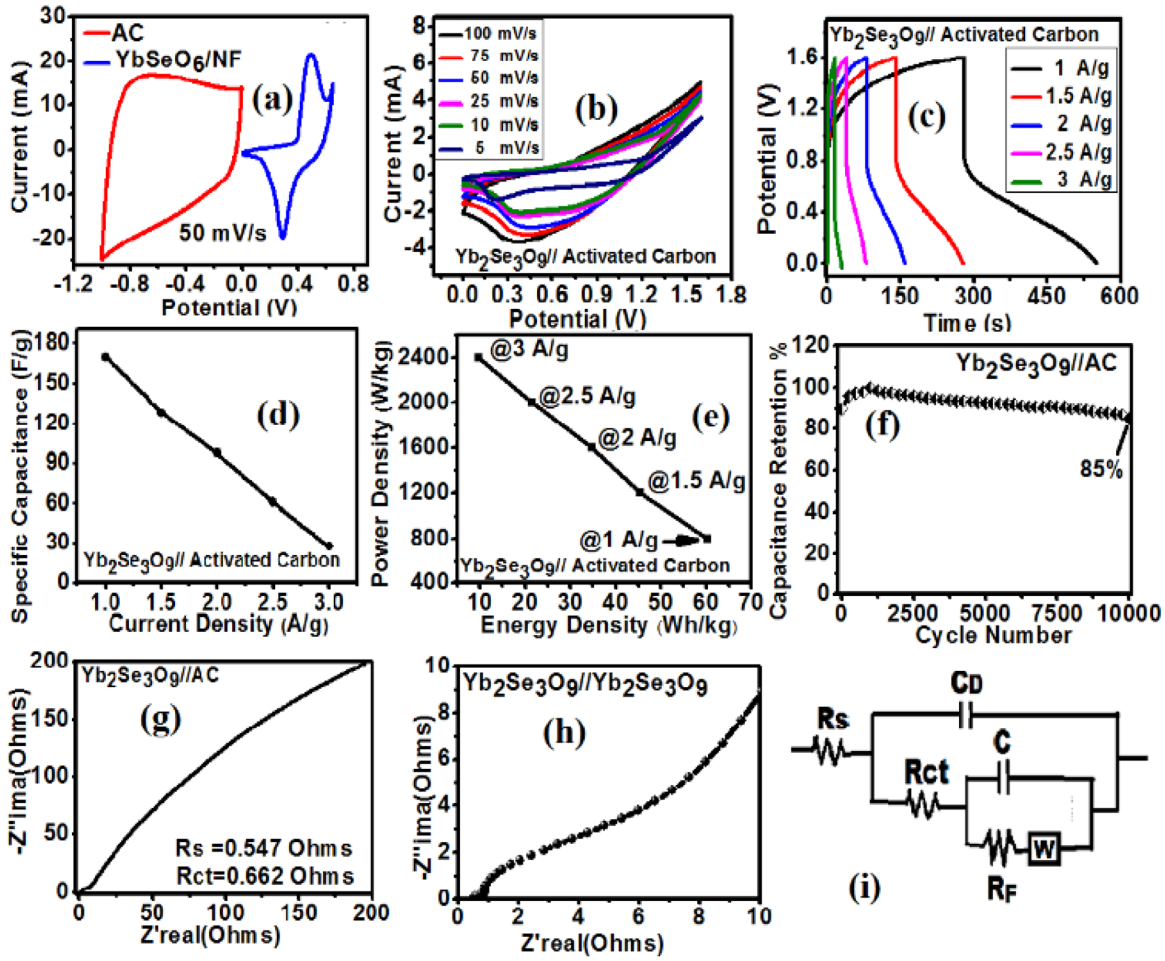


Fig. 7 (a) Comparison of CV of $Yb_2Se_3O_9$ and activated carbon of $Yb_2Se_3O_9$//AC asymmetric device to find optimal operating potential window, using a range of potential windows at a scan rate of 50 mV $s^{-1}$; (b) CV curves, (c) charge and discharge curves of asymmetric device, (d) specific capacitance *versus* current density, (e) Ragone's plot of asymmetric device, (f) cyclic stability, (g) Nyquist plot, (h) expanded Nyquist plot and (i) equivalent circuit of $Yb_2Se_3O_9$//AC.

capacitance properties and exceptional reversibility of faradaic reactions. In this instance, at densities of current 1.0, 1.5, 2, 2.5 and 3 A $g^{-1}$, specific capacities were 169.86, 128, 97.48, 60.58, and 27.42 F $g^{-1}$, respectively. Fig. 7d displays the $C_{sp}$ *vs.* current density plot. Because the electrolyte ions polarize and depolarize so quickly and reduction in the electrode surface's ability to fully utilize surface electrode for EDLC production at increased density of current, specific capacitance dropped as current densities increased. Ions of electrolyte were only transported very quickly at higher current densities, and they were unable to completely reach surface area of electrode.

Cycling durability, power and energy density, are the key considerations for investigating the practical uses of $Yb_2Se_3O_9$//AC//KOH ASC. The Ragone graph (Fig. 7e), shows energy *versus* power density for various current densities for $Yb_2Se_3O_9$ electrode. Current densities of 1.5, 2, 2.5 and 3 A $g^{-1}$ respectively, achieved densities of energy 45.51, 34.66, 21.54, and 9.75 W h $kg^{-1}$, and corresponding power densities 1200, 1600, 2000, and 2400 W $kg^{-1}$ for asymmetrical device of $Yb_2Se_3O_9$ supercapacitor with 3 M KOH. This investigation discovered a remarkable capacitance 169.86 F $g^{-1}$ between 0 V and 1.6 V, superior density of power 800 W $kg^{-1}$, and good density of energy 60.39 W h $kg^{-1}$ at 1 A $g^{-1}$.

Cyclic stability is a crucial feature of any device of supercapacitor. Furthermore, $Yb_2Se_3O_9$//AC asymmetric capacitor's cycling ability at 1.6 V was examined by GCD at 5 A $g^{-1}$ over 10 000 cycles, as in Fig. 7f. Because of its exceptional durability which reaches 85% at current discharge 5 A $g^{-1}$, high conductivity of active material with strong integration, little deterioration over numerous charge–discharge cycles, and the ability to stop structural collapse, it is a highly sought after active material for high-energy ASC devices. After the first 100 cycles, the specific capacitance decreased, which is explained by problems with pulverization and wettability. The capacitance actually increased upto 1000 cycles as a result of subsequent cycling. This is probably connected to an improvement in the electrode's surface wetting brought on by cycling, which results in a larger electroactive surface area. The asymmetric capacitor exhibits exceptional coulombic efficiency and cycle stability 10 000 cycles later. Therefore, the present study opens up a perspective for creation of fresh energy storage materials and suggests a flexible high performance asymmetric

Table 1 Analysis of performance of present work by comparing with similar rare-earth metal oxides supercapacitor devices

| Electrode/reference | Specific capacitance ($F\ g^{-1}$) | Energy density ($W\ h\ kg^{-1}$) | Power density ($W\ kg^{-1}$) | Device stability (%) | Cycle |
|---|---|---|---|---|---|
| $YbTeO_6$//$YbTeO_6$ symmetric in KOH[22] | 76.73@1 A $g^{-1}$ | 13.64 | 800 | 96.7% | 10 000 |
| $YbTeO_6$//AC asymmetric in KOH[22] | 88.36 @1 A $g^{-1}$ | 40.09 | 1000 | 80.0% | 10 000 |
| $Gd_2Se_3O_9$//$Gd_2Se_3O_9$ symmetric in KOH[20] | 48.53@1 A $g^{-1}$ | 5.70 | 650 | 77.0% | 6000 |
| $TmTeO_3$//$TmTeO_3$ symmetric in KOH[15] | 37.75@1 A $g^{-1}$ | 6.055 | 761 | 80.0% | 5000 |
| $TmSeO_3$//$TmSeO_3$ symmetric in KOH[19] | 64.60@1 A $g^{-1}$ | 30.7 | 1850 | 51.5% | 4000 |
| $Yb_2Se_3O_9$//$Yb_2Se_3O_9$ symmetric in KOH [present work] | 142.51@1 A $g^{-1}$ | 11.98 | 550 | 78.09% | 10 000 |
| $Yb_2Se_3O_9$//$Yb_2Se_3O_9$ asymmetric in KOH [present work] | 169.86@1 A $g^{-1}$ | 60.39 | 800 | 85.0% | 10 000 |

supercapacitor. The primary energy storage method in the AC electrode is an EDLC, having advantageous excellent power, energy density and extended life cycle due to high capacity rate of both positive and negative electrodes. Because asymmetric capacitors have a pseudocapacitive electrode, it's crucial to avoid turning an excellent supercapacitor into a mediocre battery.[2] These advantageous properties worked together to enable us to create high-performance electrodes, opening the door for the use of these cutting-edge materials in commercial products.[64]

Impedance study examines a resistive factor of asymmetric $Yb_2Se_3O_9$//AC device by EIS (Fig. 7g). The expanded Nyquist plot is shown in Fig. 6h. An equivalent circuit with resistance and capacitance, matching Nyquist plot is displayed in Fig. 7i. The real axis intercept, gives series resistance of $R_s$ ~0.547 Ω. Semi-arc at high frequencies gives charge-transfer resistance at electrode/electrolyte interface, $R_{ct}$ = 0.662 Ω. The presence of the RF component implies a faradaic charge-transfer event in alkali media.[53,56]

## Conclusions

Ytterbium selenite $Yb_2Se_3O_9$ has been analysed based on energy storage applications. It was prepared *via* a straightforward precipitation process. It exhibits nanorods with bamboo like structure. The particle is 110 nm in size. $Yb_2Se_3O_9$ is of monoclinic structure. It can be used as UV filters. It has energy gap 5.93 eV, Urbach energy 0.926 eV and refractive index is 1.873. It is a useful tool in the field of optoelectronics. The optical shifts between energy levels confirmed native point defects, Schottky and Frenkel surface defects presence which promotes possible application in displays and supports the radiative electron–hole recombination in $Yb_2Se_3O_9$. The presence of the Yb–O bond is confirmed by bands in fingerprint region bands. Ytterbium is in an oxide matrix in the sample. $Yb_2Se_3O_9$ reveals phase transition from 20 to 30 K under magnetic field. M–H curve of $Yb_2Se_3O_9$ at 300 K shows weak ferromagnetic characteristics. Nearly all of the ytterbium spins are aligned due to cooperative spin interaction when the applied field is 2000 Oe in field cooling. This study describes the successful construction and testing of $Yb_2Se_3O_9$ electrode devices of symmetric and asymmetric supercapacitors by employing setups with three and two electrodes in KOH electrolyte. The three electrode CV shows good symmetry and pseudocapacitor behaviour with specific capacitance 268.59 $F\ g^{-1}$ and window of operation with 0.65 V. At 1 A $g^{-1}$, chronopotentiometry produced 292.82 $F\ g^{-1}$. An electrode made of $Yb_2Se_3O_9$ was used to create a full-cell symmetric supercapacitor device. This manufactured symmetric device has high power density 550 $W\ kg^{-1}$, potential window 1.1 V, specific capacitance 142.51 $F\ g^{-1}$, and energy density 11.98 $W\ h\ kg^{-1}$ at 1 A $g^{-1}$. The cyclic stability is 78.09% specific capacitance retention at the end of 10 000 cycles. This device has good features of energy storage and conversion gadgets. Impedance study demonstrates the double-layer capacitive nature. Additionally, an asymmetric supercapacitor device constructed with KOH electrolyte, $Yb_2Se_3O_9$ positive electrode and activated carbon negative electrode demonstrated better density of power of 800 $W\ kg^{-1}$ at 1 A $g^{-1}$, an energy density of 60.39 $W\ h\ kg^{-1}$, specific capacitance of 169.86 $F\ g^{-1}$ in 1.6 V window and good capacity retention 85% after 10 000 cycles. Compared to symmetric supercapacitor, the asymmetric device demonstrated superior supercapacitive performance. As a result, the ASC device has higher specific capacitance, larger potential window, strong cycle stability, and a high energy and power density for applications of storage and conversion of energy. The electrochemical performances of the current $Yb_2Se_3O_9$ supercapacitor device are compared with those of related reported rare-earth metal oxide devices in Table 1. All of these outstanding qualities point to an alluring and straightforward path for creating innovative energy-storage materials with high energy storage capacity for the upcoming generation of electronic products.

## Data availability

Data will be made available on request.

## Author contributions

S. Shanmugha Soundare: methodology, experimental, investigation, formal analysis, data curation, conceptualization, visualization, writing – original draft, review and editing. S. Ariponnammal: methodology, investigation, conceptualization. M. Arivanandhan: writing – editing, supervision. R. Jayavel: validation, supervision, investigation, conceptualization, resources, project administration.

## Conflicts of interest

There are no conflicts to declare.

## Acknowledgements

The authors thank SAIF-IITM, Chennai, India, for access to their low temperature magnetic facilities and DST-FIST, Department of Physics, Gandhigram Rural Institute, Deemed To Be University, Gandhigram-624302, Dindigul District, Tamilnadu, India for providing XRD facility. And, authors also thank Material analysis and Research centre, Bengaluru for providing TEM facilities.

## References

1 K. S. Ahn, R. Vinodh, B. G. Pollet, R. Suresh Babu, V. Ramkumar, S. C. Kim, K. Krishnakumar and H. J. Kim, *Electrochim. Acta*, 2022, **426**, 140763.
2 R. Vinodh, R. Suresh Babu, S. Sambasivam, C. V. V. Muralee Gopi, S. Alzahmi, H. J. Kim, A. L. F. de Barros and I. M. Obaidats, *Nanomaterials*, 2022, **12**, 1511.
3 T. Susikumar, P. Justin Jesuraj, M. Navaneethan, A. Dennyson Savariraj, C. Lee and S. Y. Ryu, *Surf. Interfaces*, 2024, **55**, 105448.
4 M. Aghazadeh and H. Forati Rad, *J. Energy Storage*, 2022, **53**, 105194.
5 P. H. Patil, V. V. Kulkarni and S. A. Jadhav, *J. Compos. Sci.*, 2022, **6**, 363.
6 K. Ye, K. Li, Y. Lu, Z. Guo, N. Ni, H. Liu, Y. Huang, H. Ji and P. Wang, *Trends Anal. Chem.*, 2019, **116**, 102–118.
7 S. Ariponnammal, S. Shalini and S. Anusha, *Cryst. Res. Technol.*, 2022, **57**, 2200106.
8 U. C. Chung, J. L. Mesa, J. L. Pizarro, V. Jubera, L. Lezama, M. I. Arriortua and T. Rojo, *J. Solid State Chem.*, 2005, **178**, 2913–2921.
9 D. R. Xiao, Y. Hou, E. B. Wang, H. An, J. Lu, Y. Li, L. Xu and C. Hu, *J. Solid State Chem.*, 2004, **177**, 2699–2704.
10 I. Hentech, K. Zehani, A. Kabadou, A. Ben Salah, M. Loukil and L. Bessais, *J. Magn. Magn. Mater.*, 2017, **422**, 315–321.
11 A. Larranaga, J. L. Mesa, J. L. Pizarro, A. Pena, J. P. Chapman, M. I. Arriortua and T. Rojo, *Mater. Res. Bull.*, 2005, **40**, 781–793.
12 A. Larranaga, J. L. Mesa, J. L. Pizarro, A. Pena, R. Olazcuaga, M. I. Arriortua and T. Rojo, *J. Solid State Chem.*, 2005, **178**, 3686–3697.
13 J. H. Yoon, J. S. Bak, I. Cho, R. Vinodh, B. G. Pollet, R. Suresh Babu, H. J. Kim and S. Kim, *Molecules*, 2022, **27**, 7691.
14 R. R. Arulanantham, A. Dennyson Savariraj and V. Ragupathi, *J. Alloys Compd.*, 2025, **1022**, 179761.
15 S. Ariponnammal, N. G. Basil Ralph and S. Shanmugha Soundare, *Z. Phys. Chem.*, 2024, **258**, 2147–2164.
16 S. Liang, H. Wang, Li Yang, H. Qin, Z. Luo, B. Huang, X. Zhao, C. Zhao and L. Chen, *Sustainable Energy Fuels*, 2020, **4**, 3825–3847.
17 W. Gao, D. Wen, J. C. Ho and Y. Qu, *Mater. Today Chem.*, 2019, **12**, 266–281.
18 A. M. Haque, C. E. Alvarez-Pugliese and G. G. Botte, *ACS Sustainable Resour. Manage.*, 2024, **1**, 1377–1387.
19 S. Ariponnammal, N. G. Basil Ralph, S. Shanmugha Soundare and R. Jayavel, *Nano*, 2024, **19**, 2450021.
20 S. Ariponammal and R. Ramalakshmi, S. Shanmugha Soundare, *J. Mater. Sci.: Mater. Electron.*, 2024, **35**, 1872.
21 S. Ariponnammal, R. Ramalakshmi and S. Shanmugha Soundare, *Z. Phys. Chem.*, 2024, **239**, DOI: **10.1515/zpch-2024-0755**.
22 S. Shanmugha Soundare, S. Ariponnammal, M. Arivanandhan and R. Jayavel, *J. Appl. Electrochem.*, 2025, **55**, 2071–2091.
23 V. Muthulakshmi and M. Sundrarajan, *J. Environ. Chem. Eng.*, 2020, **8**, 103992.
24 B. Rudraswamy and N. Dhananjaya, *IOP Conf. Ser.:Mater. Sci. Eng.*, 2012, **40**, 012034.
25 M. Mazhdi and M. J. Tafreshi, *Appl. Phys. A*, 2018, **124**, 863–887.
26 M. Rahimi-Nasrabadi, S. M. Pourmortazavi, M. Aghazadeh, M. R. Ganjali, M. S. Karimi and P. Norouzi, *J. Mater. Sci.: Mater. Electron.*, 2017, **28**, 9478–9488.
27 T. Saravanan, P. Anandan, M. Shanmugam, M. Azhagurajan, M. Mohamed Ismail, M. Arivanandhan, Y. Hayakawa and R. Jayavel, *Polym. Bull.*, 2019, **77**, 1–17.
28 J. F. Moulder, W. F. Stickle, W. M. Sobol and K. D. Bomben, *Handbook of X-Ray Photoelectron Spectroscopy*, ed. J. Chastain, Perkin-Elmer Corporation, Minnesota, 1992.
29 S. Ariponnammal, S. Shalini and S. Nishanthini Devi, *Mater. Today: Proc.*, 2021, **35**, 39–43.
30 A. Rahman, K. Vasilev and P. Majewski, *J. Colloid Interface Sci.*, 2011, **354**, 592–596.
31 S. Ariponnammal and S. Anusha, *Mater. Today: Proc.*, 2022, **66**, 1606–1610.
32 C. L. Heng, C. N. Zhao, L. Zhang, W. Xiang, W. Y. Su, H. X. Yin, Y. K. Gao, P. G. Yin and T. G. Finstad, *J. Lumin.*, 2020, **222**, 117153.
33 R. K. Tamrakar, D. P. Bisen, K. Upadhyay, M. Sahu, I. P. Sahu and N. Bramhe, *Superlattices Microstruct.*, 2015, **88**, 382–388.
34 M. Piz, P. Dulian, E. Filipek, K. Wieczorek-Ciurowa and P. Kochmanski, *J. Mater. Sci.*, 2018, **53**, 13491–13500.
35 J. Mohan, *Organic Spectroscopy*, Narosa Publication House, New Delhi, 2000.
36 R. M. Silverstein and G. C. Bassler, Spectrometric identification of organic compounds, *J. Chem. Educ.*, 1962, **39**, 546.
37 K. Nakamoto, *Infrared and Raman Spectra of Inorganic and Coordination Compounds*, Wiley, New York, 1986.
38 V. P. Verma, *Thermochim. Acta*, 1999, **327**, 63–102.
39 R. A. Burley, *Mater. Res. Bull.*, 1968, **3**, 735–744.
40 P. A. Giwire and M. Falk, *Spectrochim. Acta*, 1960, **16**, 1–5.
41 S. Devanarayanan and A. Castro, *Spectrochim. Acta*, 1998, **A54**, 785–791.
42 N. J. Brassington, H. G. M. Edwards and V. Fawcett, *Spectrochim. Acta*, 1987, **43A**, 451–454.
43 J.-C. Panitz, *J. Raman Spectrosc.*, 1999, **30**, 1035–1042.
44 L. Zheng, G. Zhao, C. Yan, X. Xu, L. Su, Y. Dong and J. Xu, *J. Raman Spectrosc.*, 2007, **38**, 1421–1428.

45 R. L. Hadimani, S. Gupta, S. M. Harstad, V. K. Pecharsky and D. C. Jiles, *IEEE Trans. Magn.*, 2015, **51**, 1–4.
46 C. Sasirekha, S. Arumugam and G. Muralidharan, *Appl. Phys. A*, 2021, **127**, 124.
47 M. Sajjad, X. Chen, C. Yu, L. Guan, S. Zhang, Y. Ren, X. Zhou and Z. Liu, *J. Mol. Eng. Mater.*, 2019, **07**, 1950004.
48 W. He, C. Wang, H. Li, X. Deng, X. Xu and T. Zhai, *Adv. Energy Mater.*, 2017, **7**, 1700983.
49 Y. She, B. Tang, D. Li, X. Tang, J. Qiu, Z. Shang and W. Hu, *Coatings*, 2018, **8**, 340.
50 S. Kaba, M. M. Ndipingwi, K. V. Mokwebo, C. Nolly, K. C. Januarie, M. Oranzie, C. O. Ikpo, A. C. Nwanya and E. I. Iwuoha, *Mater. Chem. Phys.*, 2023, **305**, 127997.
51 A. D. Deshmukh, A. R. Urade, A. P. Nanwani, K. A. Deshmukh, D. R. Peshwe, P. Sivaraman, S. J. Dhoble and B. K. Gupta, *ACS Omega*, 2018, **3**, 7204–7213.
52 J. Xie, P. Yang, Y. Wang, T. Qi, Y. Lei and C. Ming Li, *J. Power Sources*, 2018, **401**, 213–223.
53 W. A. Badawy, M. M. El-Rabiei, N. H. Helal and H. M. Nady, *Z. Phys. Chem.*, 2013, **227**, 1143–1158.
54 B. A. Mei, O. Munteshari, J. Lau, B. Dunn and L. Pilon, *J. Phys. Chem.*, 2018, **122**, 194–206.
55 **https://partners/metro/hm/.com/GetDo/cumen/tPubl/ic?/action=get_dms_docum/ent&docid=20439-73**.
56 W. Choi, H. C. Shin, J. M. Kim, J. Y. Choi and W. S. Yoon, *J. Electrochem. Sci. Technol.*, 2020, **11**, 1–13.
57 E. P. Randviir and C. E. Banks, *Anal. Methods*, 2013, **5**, 1098–1115.
58 M. Tariq, *Z. Phys. Chem.*, 2019, **234**, 295–312.
59 S. B. Ubale, S. B. Kale, V. J. Mane, U. M. Patil and C. D. Lokhande, *J. Electroanal. Chem.*, 2021, **897**, 115589.
60 A. M. Abraham, S. P. Lonkar, V. V. Pillai and S. M. Alhassan, *ACS Omega*, 2020, **5**, 11721–11729.
61 S. Sharifi, K. Rahimi and A. Yazdani, *Sci. Rep.*, 2021, **11**, 8378.
62 H. Wang, M. Chris, B. Holt, Z. Li, X. Tan, B. S. Amirkhiz, Z. Xu, B. C. Olsen, T. Stephenson and D. Mitlin, *Nano Res.*, 2012, **5**(9), 605–617.
63 U. N. Pan, V. Sharma, T. Kshetri, T. I. Singh, D. R. Paudel, N. H. Kim and J. H. Lee, *Small*, 2020, **16**, 2001691.
64 S. J. Patil, A. C. Lokhande, D. W. Lee, J. H. Kim and C. D. Lokhande, *J. Colloid Interface Sci.*, 2017, **490**, 147–153.
65 D. Mandal, P. L. Mahapatra, R. Kumari, P. Kumbhakar, A. Biswas, B. Lahiri, A. Chandra and C. S. Tiwary, *Emergent Mat.*, 2021, **4**, 531–544.